

## Analysis of the surface rupture process of strong earthquakes based on centrifuge tests

Chao Shen<sup>a,\*\*</sup>, Jingshan Bo<sup>a,b,\*</sup>, Wenhao Qi<sup>b</sup>, Xuedong Zhang<sup>c</sup>, Jingyi Huang<sup>a</sup>, Feng Qiao<sup>b</sup>

<sup>a</sup> Department of Geological Engineering, Institute of Disaster Prevention, Sanhe, Hebei, 065201, China

<sup>b</sup> Key Laboratory of Earthquake Engineering and Engineering Vibration, Institute of Engineering Mechanics, China Earthquake Administration, Harbin, 150080, China

<sup>c</sup> State Key Laboratory of Simulation and Regulation of Water Cycle in River Basin, China Institute of Water Resources and Hydropower Research, Beijing, 100038, China

### ARTICLE INFO

#### Keywords:

Earthquakes  
Centrifuge model test  
Reverse fault  
Upper fault tip  
Surface deformation

### ABSTRACT

Surface ruptures caused by strong earthquakes are one of the most concerning issues for construction projects. In this paper, geotechnical centrifuge model tests is performed to successfully simulate the reverse faulting process. Using a linear laser displacement sensor (LLDS) and the particle image velocimetry (PIV) technique, the surface deformation process and faulting behaviours are studied in dry and wet sand with a thickness of 40 m above a bedrock surface. Based on an analysis of high-precision surface monitoring data, the soil rupture process is divided into four stages: the overall uplift period, inclination deformation period, scarp growth period, and deformation slowdown and lag period. In addition, the characteristics of the soil deformation and the propagation behaviour of the upper fault tip are obtained. This experiment and related achievements can provide references for further understanding the deformation of thick soil layers caused by reverse faulting.

### 1. Introduction

The neotectonic activity in China is strong, and strong earthquakes can rupture the surface; moreover, as active faults are widely distributed, various long-distance linear engineering projects are being constructed across faults [1]. Movement along a fault associated with a strong earthquake can rupture and deform the surface, causing great damage to structures (such as buildings on the surface), underground pipelines and tunnels and seriously threatening people's lives and property [2]. As examples, the magnitude 7.6 Chi-Chi earthquake in 1999 and the magnitude 8.0 Wenchuan earthquake in 2008 caused large-scale surface ruptures, and numerous dam foundations, road bridges and underground pipelines were damaged [3].

For active faults exposed directly at the surface, relevant studies have presented empirical formulas describing the relationship among the earthquake magnitude, displacement, active fault length and slip rate [4–6]. Nevertheless, it remains challenging to evaluate the extent of the influence of the surface rupture zone resulting from movement along a concealed fault and to understand the geometric and kinematic characteristics of surface rupture zones caused by concealed faults in future earthquake events. Therefore, this issue, which requires further

exploration, continues to constitute a major focus of active fault evaluations [7]. In particular, with the development of active fault detection systems in cities, it is urgently necessary to provide both a basis for evaluating the surface ruptures of strong earthquakes and a method to evaluate the geometric and kinematic characteristics of surface rupture zones for engineering construction projects.

Numerous previous studies have addressed these problems via post-earthquake survey statistics [8,9], the 1g sandbox model test method [10,11], the numerical simulation method [12,13] and the geotechnical centrifuge test method [14,15]. Unfortunately, due to the lack of measurements of the damage caused by surface ruptures, a large number of experiments are needed to obtain relevant data. In the natural world, the overlying soil layer can be as thick as several tens of metres or even hundreds of metres. Only at high-g centrifugal accelerations can a small-scale physical model be generated that can realistically reflect the stress state under natural conditions and simulate the natural change process of soil at different depths; thus, the geotechnical centrifuge test is favoured by researchers in China and elsewhere.

Previous studies that conducted centrifuge tests of reverse faults mainly investigated the deformation characteristics of different types of soil and the impacts of soil compaction and soil-structure interaction.

\* Corresponding author. Department of Geological Engineering, Institute of Disaster Prevention, Sanhe, Hebei, 065201, China.

\*\* Corresponding author.

E-mail addresses: [shenchao@cidp.edu.cn](mailto:shenchao@cidp.edu.cn) (C. Shen), [bjs@cidp.edu.cn](mailto:bjs@cidp.edu.cn) (J. Bo).

However, it difficult to obtain continuous deformation characteristics of the soil due to the low monitoring accuracy, the sparsity of surface monitoring points, and the broad spacing between two adjacent monitoring points; consequently, most previous studies offered only qualitative conclusions that could not be analysed quantitatively. In addition, fewer centrifuge tests have been applied to reverse faults than to normal faults, and the simulated maximum thickness of a reverse fault is smaller than that of a normal fault [16]. The main reason may be that reverse fault centrifuge simulation tests need to overcome a force of  $n$  times the gravity generated by the overlying soil under high- $g$  loading, which imposes strict requirements on the stability of the simulator and relative equipment; furthermore, because additional uncertain factors are present, this requirement will be very difficult to achieve. In this experiment, a self-designed reverse fault simulation device and the geotechnical centrifuge simulation technique are used to successfully increase the simulated thickness of the soil overlying a reverse fault to approximately 40 m. At the same time, by using a high-precision linear laser displacement sensor (LLDS) and a high-speed camera during deformation, continuous and accurate depictions of the soil deformation process are obtained. Accordingly, the data presented in this study further reveal the characteristics of the changes in soil caused by reverse faulting.

## 2. Test equipment and method

### 2.1. Introduction to the centrifuge and instrument layout

The experiment is performed in the geotechnical centrifuge at the China Institute of Water Resources and Hydropower Research (IWHR), as shown in Fig. 1a. The centrifuge has a payload of 1.5 t, an effective radius of 5.03 m, a capacity of 450 g-ton, and a test basket size of 1.5 m  $\times$  1.0 m  $\times$  1.5 m (length  $\times$  width  $\times$  height). The centrifugal acceleration used in this reverse faulting test is 100g, so the ratio between the model and prototype dimensions is 1:100.

After the soil sample is prepared, it is hoisted into the centrifuge basket. Two digital high-definition (HD) cameras (Fig. 1b) are installed on the inner side of the basket and the top of the model box to record the soil deformation and fracture (fault) propagation in real time. The recording speed at which these HD cameras monitor the deformation and faulting of the soil profile in real time is 5 frames/s. Additionally, the displacement fields during different soil deformation periods are calculated and analysed by the particle image velocimetry (PIV) technique [17]. The LLDS (shown in Figs. 1b–2b) is placed at the centre of the top of the model box to monitor the surface changes in real time. The sampling interval is approximately 0.05 s, and the sampling point

spacing of the linear laser is 0.25 mm. The number of effective sampling points in dry sand is 872, and that in wet sand is 928; thus, deformation processes in the range of 21–23 cm on the surface of the soil can be obtained accurately.

### 2.2. Centrifuge test procedure

According to the statistics of reverse fault centrifuge tests conducted over the years, the dip angle of the reverse fault in centrifuge tests is typically set between 45° and 60° [16]. In addition, based on the statistics of faults in China, the fault dip is concentrated mostly between 50° and 70° [2]. Therefore, a dip angle of 60° is selected for the fault plane in this test. On the one hand, this dip angle makes it easy to compare and analyse these results with those of previous reverse fault centrifuge tests under the same fault dip; on the other hand, the chosen dip angle is in accordance with the actual situation and therefore has broad representativeness. Accordingly, a hydraulic jack is employed to set the bottom of the model box to an angle of 60° relative to the horizontal to simulate the reverse faulting process. The maximum lift of the jack is 5 cm, and the average rate of uplift is approximately 0.26 cm/s at 100g. Table 1 shows the basic similarity laws of the centrifuge model's physical parameters. According to the imposed centrifugal acceleration, the imposed bedrock offset is 5 m, so the maximum vertical displacement is 4.33 m.

The centrifuge test is divided into the following four steps. ①The centrifuge enters the acceleration phase and reaches the target value of 100g after approximately 20 min. During the transition from 1g to 100g, the LLDS is turned on to obtain the surface subsidence caused by the increase in the  $g$  value. ② When the centrifugal acceleration reaches 100 g, the model is allowed to consolidate for 10 min ③The two cameras and the LLDS are turned on to obtain relevant images and data. Then, the hydraulic pump is switched on to drive the jack and push the hanging wall to simulate the reverse fault displacement process until the maximum offset reaches 5 cm ④ After the completion of the simulation test, the machine is shut down, the model box is unloaded, and model observations and analysis are subsequently carried out.

## 3. Model design and soil preparation

The test model box is rectangular (Fig. 2a) with internal dimensions of 132 cm  $\times$  41 cm  $\times$  80 cm (length  $\times$  width  $\times$  height), and the simulator is made of aluminium alloy plates to simulate the hanging wall of a reverse fault with a dip angle of 60°. The foot wall on the right remains stationary during the test. The middle of the front of the model box consists of a transparent observation window with dimensions of 76 cm



(a) Geotechnical centrifuge at the IWHR

(b) Equipment in the hanging basket

Fig. 1. Test equipment and monitoring arrangement.

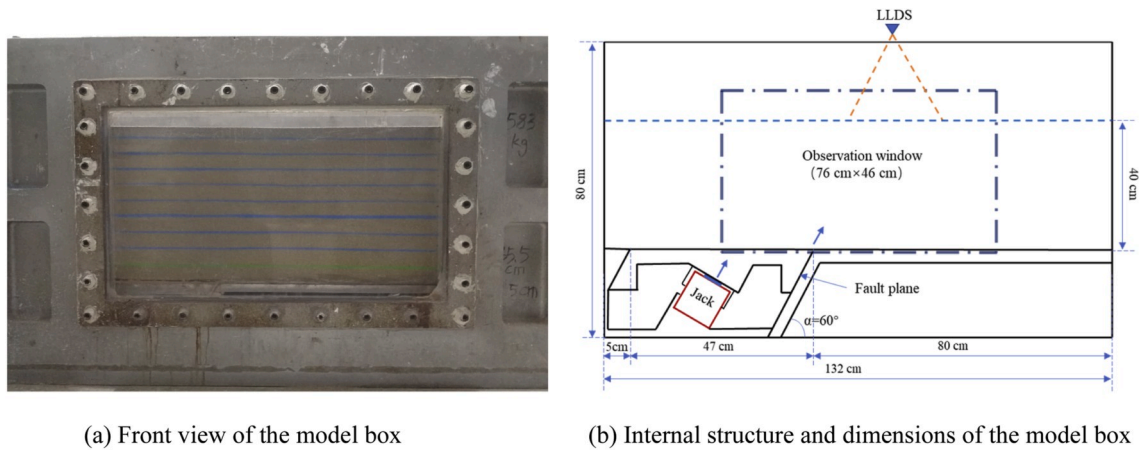


Fig. 2. Schematic diagram of the model box and simulator.

**Table 1**  
Basic similarity laws of the centrifuge model's physical parameters [18].

Physical quantity	Length	Area	Volume	Stress	Strain	Displacement	Quality	Acceleration	Energy
Model	1/n	1/n <sup>2</sup>	1/n <sup>3</sup>	1	1	1/n	n <sup>3</sup>	n	n <sup>3</sup>
Simulation	1	1	1	1	1	1	1	1	1

× 46 cm (length × width), through which it is possible to clearly observe the internal soil change process.

In this test, the weight of the soil is 343 kg, so the total weight of the overlying soil can reach 34.3 t at 100g. To successfully achieve the stable lifting of the soil at such a high g value, the load on the top of the jack and the resistances caused by various contact surfaces should be reduced as much as possible. Therefore, the rising disc boundary in the fault simulation device is simplified (Fig. 2b); that is, the rising wedge-shaped boundary used in previous experiments is not adopted [19]. The advantage of this simplified treatment is that it can minimize the load on top of the jack and further increase the thickness of the soil while reducing the frictional resistance generated by areas of contact during the lifting process; the disadvantage is that the soil within a certain distance from the left end of the model box will deform accordingly. However, subsequent measurements reveal that this simplified treatment affects the soil only within 20 cm (the prototype is 20 m) from the left boundary of the model box. The length of the soil model in this experiment is 1.32 m, and thus, the model can simulate 132 m at 100g, indicating that the edge of the disturbed soil at the left end will be approximately 60 cm (the prototype is 60 m) from the surface rupture of the reverse fault being investigated. According to the results of field investigations, the damage occurring outside the range of 20–30 m on either side of the surface rupture zone of a strong earthquake will be significantly reduced [20,21]; therefore, the deformation of the soil near the left end of the model box will not affect the soil within the monitoring range. In addition, the laser monitoring data during the test show that the soil surface within the monitoring range continues to rise steadily without interruption or anomaly. In summary, the simplified processing scheme employed for this kind of boundary is feasible when the model box is sufficiently long (the length should exceed 1 m).

The specimens are prepared by simulating rainfall on the sand from a specific height with a controllable mass flow rate to create homogeneous conditions in the sand. In this experiment, two types of soil samples, dry sand and wet sand, are prepared, and the water contents are 0.1% and 6%, respectively. After preparation, the soil model dimensions are 132 cm × 41 cm × 40 cm (length × width × height), and according to the centrifugal acceleration, the prototype dimensions are 132 m × 41 m (length × width) at 100g. Consolidation and settlement occur in the soil model from 0g to 100g; therefore, the basic physical parameters of the

soil also change due to the corresponding decrease in soil volume. The final physical parameters of the soil samples and the depth of the simulation are listed in Table 2. The amount of non-dimensional bedrock offset is defined as  $C=(h_v/H_0) \times 100\%$ , where  $h_v$  is the vertical bedrock offset,  $H_0$  is the soil thickness after consolidation and stable settlement at 100g,  $h_{max}$  is the maximum bedrock offset,  $h_{v-max}$  is the maximum vertical bedrock offset, and  $d_{50}$  is the median diameter of the sand. It should be noted that in the wet sand centrifuge test, a small amount of sand begins to leak downwards along the lateral wall of the model when the rising disc is moved to  $h = 4.6$  cm. To ensure the reliability of the data, all subsequent monitoring data are discarded; therefore, the maximum bedrock offset of wet sand does not reach the designed maximum.

#### 4. Evolution of the deformation and failure of the overburden layer caused by faulting

##### 4.1. Establishment of the soil model coordinate system

To analyse the deformation behaviours of the soil and upper fault tip, this paper establishes a Cartesian coordinate system with the base of the fault plane at point O as the coordinate origin, as shown in Fig. 3. The intersection between the extension of the fault plane and the surface is point F, which is 23 m from O'. As the amount of imposed bedrock offset increases, the fault plane gradually develops upward; point A represents the upper tip of the fault plane, the slope angle of the surface deformation is  $\beta$ , and the intersection between the slope and the original horizontal plane (the undeformed surface) is point N. The analysis of all test results below is described based on the prototype dimensions.

Fig. 4 shows high-resolution photographs of the final deformation of the soil at 100g. The rupture evolution of both dry sand and wet sand is analysed by comparing a series of photographs of the deformation in profile view.

##### 4.2. Evolution of soil deformation and failure

The duration of faulting is 19 s. The bottom jack does not provide a constant rate of uplift at 100g; the rate of uplift is slower (approximately 0.2 cm/s) during the first and last 6 s, while the maximum rate of uplift is approximately 0.33 cm/s, and the average rate is 0.26 cm/s. Because the

**Table 2**  
Parameters of the reverse fault simulation test (in prototype dimensions).

Soil sample	g level	Water content (%)	Density (g/cm <sup>3</sup> )	Dr (%)	d <sub>50</sub> (mm)	h <sub>max</sub> (m)	h <sub>v-max</sub> (m)	C <sub>max</sub> (%)	H <sub>0</sub> (m)
Dry	100	0.1	1.61	80	0.5	5	4.33	11.1	39.03
Wet	100	6	1.63	83	0.5	4.6	4	10.1	39.35

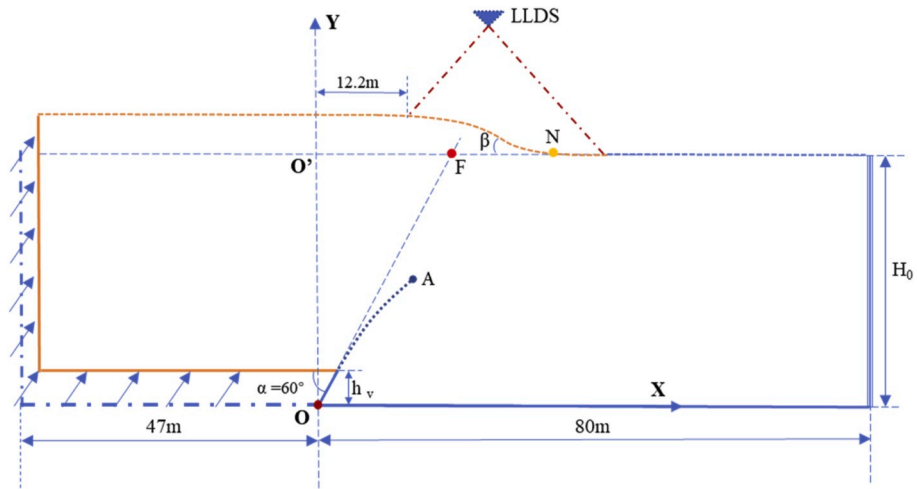
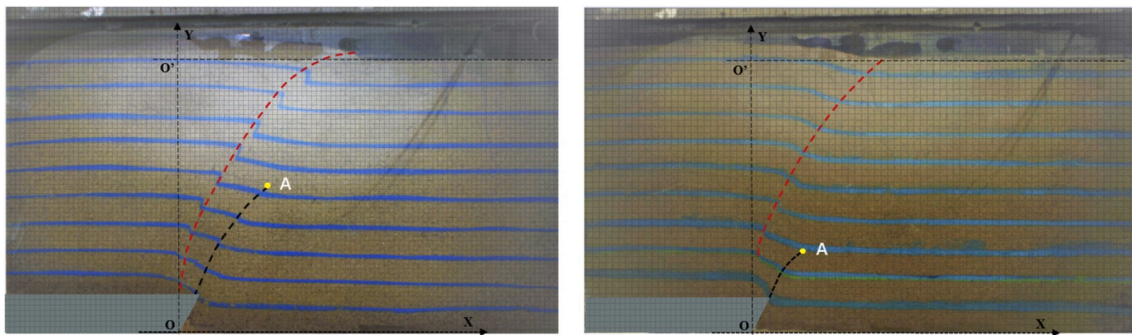


Fig. 3. Schematic diagram of the soil model coordinates for the reverse fault centrifuge test (in prototype dimensions).



(a) dry sand

(b) wet sand

Fig. 4. Final deformation photographs of dry sand and wet sand in profile view at 100g

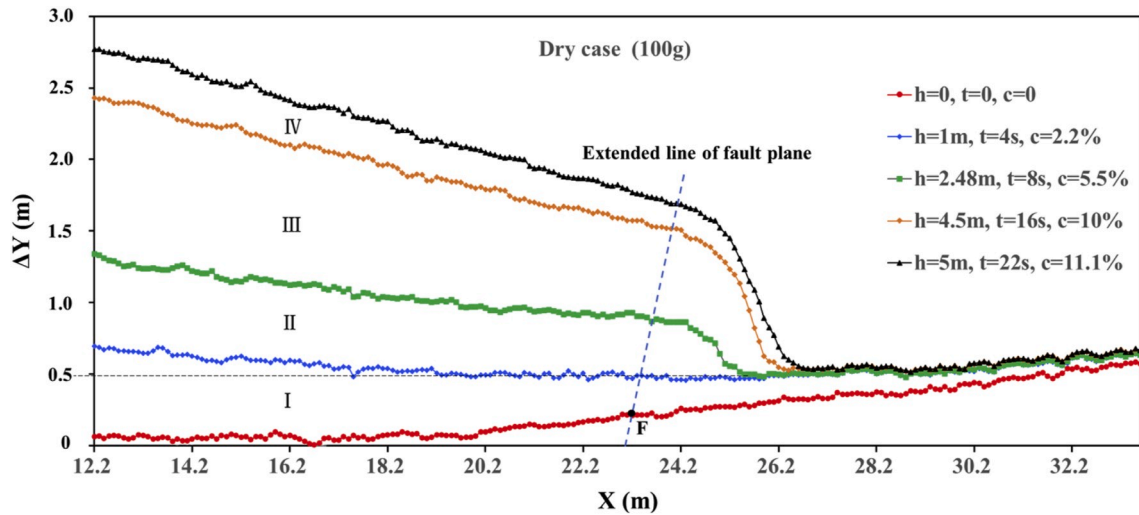


Fig. 5. Deformation contours of the dry sand surface in different stages (in prototype dimensions).

maximum amount of imposed offset in the wet sand test does not reach the designed maximum, no monitoring data from the wet sand test are retained after 17 s. In this paper, the line connecting the inflection points in the blue layers in the soil is regarded as the fault plane through the soil (Fig. 4). According to the deformation of the dry sand surface and the evolution of the fault plane, the deformation of deep soil can be divided into the following four stages (Fig. 5).

Overall uplift period (stage I): The first fault plane develops upward until the second fault plane appears, and the duration is  $0 \leq t < 4$  s (Fig. 6a and b). In this stage, the surface experiences overall uplift, but

the surface does not obviously deform. The maximum surface elevation is less than the amount of imposed offset, and the soil exhibits compaction, which corresponds to the quasi-elastic deformation phase described by I. Anastasopoulos [13]. The fault plane at the bottom of the soil extends upward along the direction of the fault plane within the bedrock. When the fault plane reaches a certain depth, the dip angle decreases, and when the upper fault tip reaches point  $A_1$  ( $x_1 = 7$  m,  $y_1 = 13$  m), a second fault plane appears to the upper left of the bedrock fault plane.

Inclination deformation period (stage II): The duration of this phase

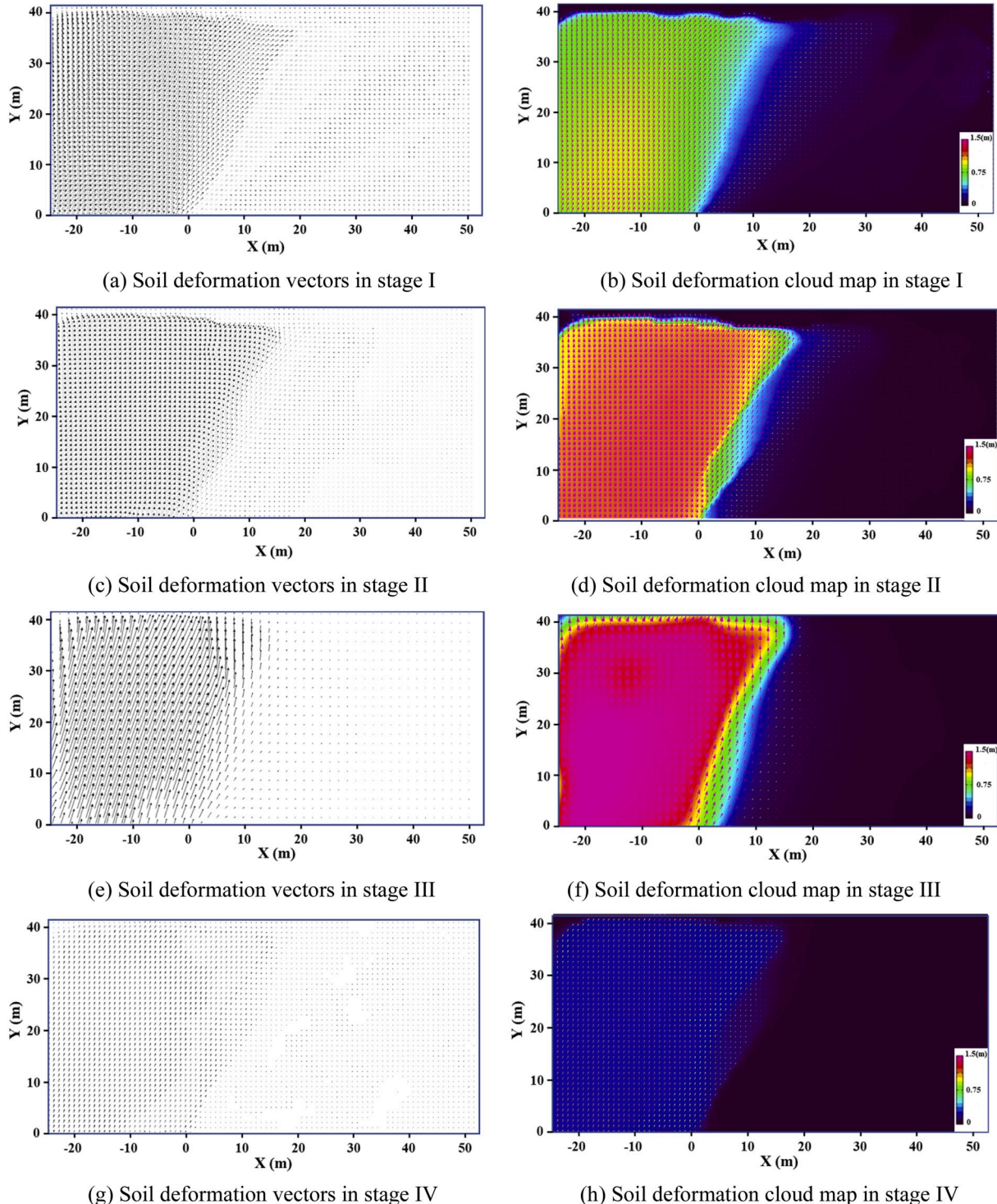


Fig. 6. Deformation of the dry sand during the reverse faulting at 100g

is  $4 \text{ s} \leq t < 8 \text{ s}$  (Fig. 6c and d). During this period, the second fault plane extends until it penetrates the surface. At  $t = 4 \text{ s}$ , the second fault plane appears, and the first (lowest) inflection point appears on the surface and begins to produce deformation. A comparison and analysis of the real-time photographs captured by the HD camera reveal that the two fault planes develop upward at the same time, but the second fault plane propagates much faster than the first plane. When the upper tip of the second fault plane reaches the surface, a scarp appears; at this moment, the first fault plane extends to point  $A_2$  ( $x_2 = 14 \text{ m}$ ,  $y_2 = 22 \text{ m}$ ) and then stops extending.

Scarp growth period (stage III): The duration of this phase is  $8 \text{ s} \leq t < 16 \text{ s}$  (Fig. 6e and f). During this period, the imposed offset and surface uplift rate increase steadily and uniformly; furthermore, the surface scarp grows, becoming increasingly obvious, and gradually shifts relative to the footwall. In addition, when the second fault plane reaches the surface, the soil already exhibits general shear failure, so the propagation of the first fault plane gradually ceases. The final exposed position of the second fault is the uppermost inflection point of the surface scarp.

Deformation slowdown and lag period (stage IV): The duration of this phase is  $16 \text{ s} \leq t < 22 \text{ s}$  (Fig. 6g and h). At this stage, the deformation rate of the surface slows because the imposed offset produced by the jack is slower than in the previous stages. It is worth noting that the imposed bedrock offset terminates at 19 s, but the surface deformation ceases at 22 s, demonstrating that the surface deformation has a certain hysteresis effect. In this stage, the shapes of the two fault planes in profile view do not change.

To further investigate the deformation and failure of the soil, the PIV technique is applied to obtain the corresponding deformation vectors of the dry sand at different deformation stages (Fig. 6). The figure indicates that for the soil at the same depth, the displacement vector at each point decreases gradually from the hanging wall to the foot wall (from left to

right), and the angle between the displacement vector and the horizontal plane gradually decreases. For soils at different depths, the displacement vector at each point gradually decreases from bottom to top, and the angle between the displacement vector and the horizontal plane gradually increases and even shifts vertically upward close to the Earth's surface. The interior of the soil can be divided into three areas at the onset of displacement at the bottom of the soil. The hanging wall on the left is the overall uplift zone, the coloured transition zone in the middle can be regarded as the shear zone, and the black zone on the right is the static zone of the footwall. This conclusion is consistent with the results of Yulong Chen [22]. However, significant partitioning occurs at the beginning of the experiment but does not occur after the deformation is terminated.

## 5. Analysis of the characteristics of soil deformation and faulting

Continuous contours of the surface deformation of dry sand and wet sand are obtained by processing the high-precision data obtained by the LLDS (Fig. 7), and these data are compared with the real-time profiles corresponding to the different imposed offsets. The following characteristics are found.

### 5.1. Surface deformation characteristics

The moment before the hydraulic jack begins to lift at 100g, the surface is slightly tilted. The reason for this minor deformation may be that the surface of the soil gradually becomes perpendicular to the ground during the rotation of the centrifuge, and the soil is slightly affected by the gravity of the Earth during this period, so the surface shows a slight inclination. The slope of the dry sand is approximately

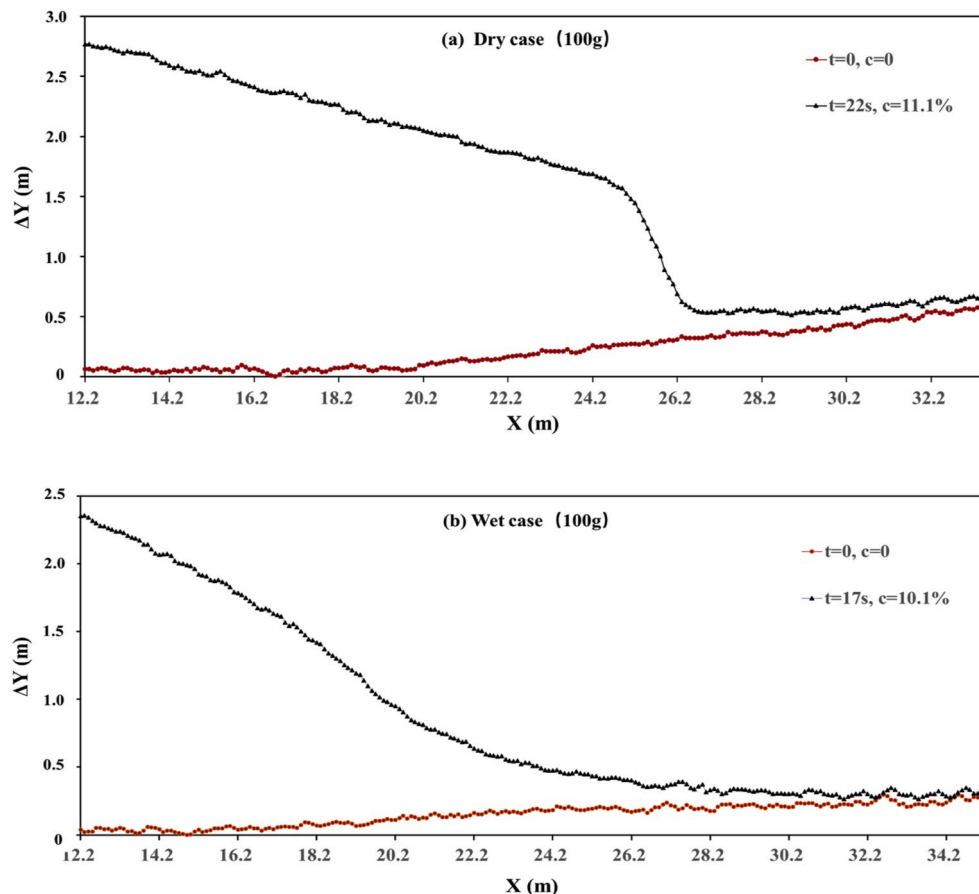


Fig. 7. Comparison of the surface deformation profiles before and after the reverse faulting of dry sand and wet sand.

1.3° (Fig. 7a), and that of the wet sand is approximately 0.5° (Fig. 7b). The wet sand is less affected by gravity than the dry sand, possibly due to the larger internal friction angle of the wet sand and capillary cohesion.

In the surface deformation process, the final surface profile of the dry sand obviously displays a scarp, and the upper and lower inflection points are evident. When the vertical offset accounts for approximately 2.2% of the soil thickness, the surfaces of the dry sand and wet sand both begin to tilt. When the deformation of the dry sand surface stops, the final position of the lower inflection point is located approximately 27 m from point O', while the upper inflection point corresponds exactly to the second fault plane at the surface. The final profile of the wet sand surface is relatively flat with no obvious inflection point. In the range of the LLDS during the displacement process, the overall uplift of the dry sand surface is 2.8 m, and that of the wet sand is 2.3 m.

### 5.2. Propagation characteristics of the upper tip of the fault plane

The overlying soil layer is divided into a hanging wall and a foot wall by the line representing the bedrock fault plane. Most of the displacement occurs in the hanging wall (Fig. 6). There is more than one internal fault plane within the soil. The dry sand and wet sand both produce two fault planes; these two faults extend upward, and the dip angle gradually decreases. As they propagate upward, the fault planes become inclined towards the foot wall, and the second fault plane is eventually exposed at the surface (Fig. 4), which is consistent with the findings of K.J.L. Stone [23]. In addition, based on the evolution of the fault plane and the surface profile, three phenomena that have never been mentioned in previous centrifuge tests are discovered.

First, when the second fault plane appears, the lower inflection point clearly appears in the surface of the dry sand. Meanwhile, the surfaces of both the dry sand and the wet sand begin to tilt. From a surface perspective, the fault can be considered to rupture the surface at this time. However, observations of the soil profile reveal that the upper marker layer is not ruptured. Strictly speaking, the surface only begins to produce oblique deformation, but the upper fault tip does not reach the surface. In the dry sand, when the surface shows an upper inflection point, the second fault plane reaches the surface, and the upper inflection point happens to reflect the outcrop at the upper fault tip.

Second, when the second fault plane appears, the speed at which the upper tip of the first fault plane extends upwards is significantly slower than before the second fault appears. Finally, when the second fault plane reaches the surface, the first fault plane stops developing. The reason may be that when the second fault plane reaches the surface, the energy is released through the deformation of the surface, so the first fault plane stops propagating.

Third, the propagation speed of the second fault plane is significantly faster than that of the first fault plane, mainly because the first fault gradually ceases to develop when the second fault reaches the surface. For the dry sand, the surface scarp shifts to the right after the upper inflection point appears on the surface.

To obtain the area affected by the surface deformation, the surface slope angle is determined by a series of secant lines of the final surface profile. The point on the right side of point F with a slope angle close to 0° is regarded as point N, which is also regarded as the boundary of the surface scarp in the established coordinate system (Fig. 3). Table 3 summarizes the test results of the upward propagation of the upper tips of the two fault planes. In Table 3,  $(x_1, y_1)$  are the coordinates of point A<sub>1</sub>, which represents the position of the upper tip of the first fault plane when the second fault plane appears, and  $(x_2, y_2)$  are the coordinates of point A<sub>2</sub>, which is the final position of the upper tip of the first fault plane when the second fault plane reaches the surface of the dry sand. In contrast, the deformed surface of the wet sand is relatively flat, and hence, there is no corresponding inflection point.

**Table 3**

Comparison of the test results regarding the fault planes in the dry sand and wet sand.

Soil	Fault plane	A <sub>1</sub> (x <sub>1</sub> , y <sub>1</sub> ) (m)	A <sub>2</sub> (x <sub>2</sub> , y <sub>2</sub> ) (m)	∠O'NO (°)	β (°)	C <sub>1</sub> (when the second fault appears)	C <sub>2</sub> (when the second fault outcrops at the surface)
Dry	Fault 1	(7, 13)	(14, 22)	55.3	0–31.3	3.3%	5.5%
	Fault 2	–	–				
Wet	Fault 1	(5, 8)	(6, 10)	52.7	0–12.2	5.6%	7%
	Fault 2	–	–				

### 5.3. Shear zone variation characteristics

In this paper, the coloured transition zone, that is, the transition between the hanging wall and foot wall in the soil deformation cloud map, is regarded as the shear zone. With an increase in the imposed offset and the appearance of the second fault plane, this zone exhibits a certain pattern of change. The shear zone develops upward along the dip direction of the bedrock fault plane in stage I. The development trend of the shear zone is basically consistent with the fault plane. The angle of upward propagation of the shear zone gradually decreases near the surface. During the overall uplift period, especially when the imposed offset is small, the shear zone pattern resembles a trumpet, and a "V" shape is formed (Fig. 6a and b). This phenomenon is consistent with the results of Y.Y. Chang [24].

In stage II, due to the appearance of the second fault plane, the deformation mode deep within the soil changes, and there are obvious borders for the shear zone, so the colour changes suddenly; this corresponds to the second fault plane. The shape of the shear zone also changes: the bottom of the shear zone is sandwiched between the two fault planes, and the hanging wall of the soil is bounded by the second fault plane. Because the first fault plane stops developing at A<sub>2</sub>, the right boundary of the shear zone is not obvious above point A<sub>2</sub> (Fig. 6d).

In stage III, the imposed bedrock offset is the largest, and the displacement vector at each point within the soil body is vertically upward in the region where the second fault plane is close to the surface (Fig. 6e); the corresponding surface uplift is also the largest. With increasing surface uplift, the shear zone gradually shifts towards the right, although the width and shape of the shear zone remain almost unchanged. The surface scarp also translates towards the right. This stage leads mainly to large relative vertical displacements of the soils on both sides of the shear zone. This conclusion is consistent with the test results of Guanyong Luo [25].

In stage IV, the surface exhibits a small amount of deformation, but the shape of the shear zone does not change greatly. The bottom boundary of the shear zone is basically coincident with the two fault planes, and the boundary of one side of the hanging wall coincides with the second fault plane. The first fault plane stops developing after stage II, so the boundary of the right-upper part of the shear zone is not obvious, and the overall shape of the shear zone resembles a reverse tilted "✓" shape.

## 6. Conclusion

In this paper, the deformation of soil within 40 m of a reverse fault is simulated by a centrifuge model test at 100g, and the deformation characteristics of dry and wet sand resulting from a bedrock fault with a dip angle of 60° are obtained. The results can provide references for further understanding the failure mechanism of soil overlying a concealed reverse fault. The following main research conclusions are drawn.

- (1) At the beginning, the surface is in an overall uplift stage, and a scarcely obvious scarp is observed. At this moment, the soil comprises three distinct zones: the hanging wall uplift zone, foot wall quiescent zone and intermediate shear zone. The surface begins to deform when the amount of imposed offset accounts for approximately 2.2% of the thickness of the soil.
- (2) The surface deformation in the dry sand is more intense than that in the wet sand. Upper and lower inflection points are generated in the dry sand, forming a surface slope, while the final surface profile of the wet sand surface is relatively gentle, so the surface scarp in the wet sand is less obvious. According to the characteristics of the surface deformation, the surface deformation is divided into four stages, namely, the overall uplift period, inclination deformation period, scarp growth period and deformation slowdown and lag period.
- (3) The propagation behaviours of the fault planes in the soil are obtained by analysing the profile deformation views. The following characteristics are observed. ① There are two fault planes in the dry sand and the wet sand, and the second fault plane extends to the surface. ② When the second fault plane appears, the first fault plane gradually stops developing. ③ The second fault plane develops more rapidly than the first fault plane, and the dip angle gradually decreases as the two fault planes develop upward.
- (4) The displacement at each point in the soil at different depths along the same vertical line gradually decreases from the bottom to the top, and the deformation vector gradually becomes steeper. The displacement at each point in the soil at the same depth gradually decreases from the hanging wall to the foot wall (from left to right), and the displacement vector gradually becomes shallower.
- (5) The shape and extent of influence of the shear zone also constantly change with increasing offset. During the overall uplift period, the boundaries of shear zone are not obvious. When the second fault plane reaches the surface, the boundaries of the shear zone are consistent with the two fault planes; thus, because the first fault plane does not reach the surface, the shear zone eventually presents a reverse tilted "✓" shape.

#### Data availability

The data used to support the findings of this study are included within the article.

#### Declaration of competing interest

We declare that there are no conflicts of interest regarding the publication of this paper. We do not have any commercial or associative interest that represents a conflict of interest in connection with the work submitted.

#### CRedit authorship contribution statement

**Chao Shen:** Conceptualization, Methodology, Writing - original draft, Data curation, Software. **Jingshan Bo:** Methodology, Writing - review & editing, Supervision. **Wenhao Qi:** Validation, Investigation. **Xuedong Zhang:** Project administration, Visualization. **Jingyi Huang:** Supervision, Resources. **Feng Qiao:** Software.

#### Acknowledgements

This work formed part of the project entitled "Urban active fault detection and seismic hazard assessment: Centrifuge test study on fault behaviour" (20180004), which was supported by the China Earthquake Administration (CEA), Department of Earthquake Defence. This was also funded by the National Natural Science Foundation of China

(U1939209). The authors would like to express their gratitude for the financial and technical support that has made this study and future research possible.

#### Appendix A. Supplementary data

Supplementary data to this article can be found online at <https://doi.org/10.1016/j.soildyn.2020.106239>.

#### References

- [1] Zhou Zhenhua, Zhang Yangmei, Sun Pingshan, et al. A summary of damage study on fault site. *Earthq Eng Vib* 2003;23(5):38–41. <https://doi.org/10.13197/j.eeev.2003.05.006>.
- [2] Huang Jingyi, Bo Jingshan, Shen Chao, et al. Progress in research on engineering evaluation of surface ruptures in strong earthquakes. *J Nat Disasters* 2016;25(6):94–104. <https://doi.org/10.13577/j.jnd.2016.0612>.
- [3] Dong JJ, Wang CD, Lee CT, Liao JJ, Pan YW. The influence of surface ruptures on building damage in the 1999 Chi-Chi earthquake: a case study in Fengyuan City. *Eng Geol* 2004;71(1–2):157–79. [https://doi.org/10.1016/S0013-7952\(03\)00131-5](https://doi.org/10.1016/S0013-7952(03)00131-5).
- [4] Deng Qidong, Yu Guihua, Ye Wenhua. *Relationship between earthquake magnitude and parameters of surface ruptures associated with historical earthquakes*. Beijing: Seismological Press; 1992. p. 247–64.
- [5] Wells Donald L, Kevin J, Coppersmith. New empirical relationships among magnitude, rupture length, rupture width, rupture area, and surface displacement. *Bull Seismol Soc Am* 1994;84(4):974–1002. <https://doi.org/10.1007/BF00808290>.
- [6] Hu Ping, Ding Yanhui, Cai Qipeng, et al. Centrifuge modelling on the behaviour of co-seismic fault dislocation in the Quaternary stratum. *Chin J Geophys* 2011;54(9):2293–301. <https://doi.org/10.3969/j.issn.0001-5733.2011.09.012>.
- [7] Han Zhujun, Ran Yongkang, Xu Xiwei. Primary study on possible width and displacement of future surface rupture zone produced by buried active fault. *Seismol Geol* 2002;24(4):484–94. <https://doi.org/10.3969/j.issn.0253-4967.2002.04.002>.
- [8] Zhou Qing, Xu Xiwei, Yu Guihua. Investigation on widths of surface rupture zones of the M8.0 Wenchuan earthquake, Sichuan province, China. *Seismol Geol* 2008;30(3):778–87. <https://doi.org/10.3969/j.issn.0253-4967.2008.03.016>.
- [9] Lin MingLang, Chung ChunFu, Jeng FuShu. Deformation of overburden soil induced by thrust fault slip. *Eng Geol* 2006;88(1–2):70–89. <https://doi.org/10.1016/j.enggeo.2006.08.004>.
- [10] Cole David A, Lade Poul V. Influence zones in alluvium over dip-slip faults. *J Geotech. Eng.* 1984;110(5):599–615. [https://doi.org/10.1016/0148-9062\(84\)92778-5](https://doi.org/10.1016/0148-9062(84)92778-5).
- [11] Johansson Jörgen, Konagai Kazuo. Fault induced permanent ground deformations-an experimental comparison of wet and dry soil and implications for buried structures. *Soil Dynam Earthq Eng* 2006;26(1):45–53. <https://doi.org/10.1016/j.soildyn.2005.08.003>.
- [12] Zhao Lei, Xiaojun LL, Huo Da. Numerically simulate the response Complexion of the overlying soil with soft interlayer due to fault bedrock dislocation. *J Beijing Univ Technol* 2007;33(3):289–92. <https://doi.org/10.3969/j.issn.0254-0037.2007.03.013>.
- [13] Anastasopoulos I, Gazetas G, Asce M, et al. Fault rupture propagation through sand: finite-element analysis and validation through centrifuge experiments. *J Geotech Geoenviron Eng* 2007;133(8):943–58. [https://doi.org/10.1061/\(asce\)1090-0241](https://doi.org/10.1061/(asce)1090-0241).
- [14] Roth WH, Scott RF, Austin I. Centrifuge modelling of fault propagation through alluvial soils. *Geophys Res Lett* 1981;8(6):561–4. [https://doi.org/10.1016/0148-9062\(82\)91726-0](https://doi.org/10.1016/0148-9062(82)91726-0).
- [15] Ng CWW, Cai QP, Hu P. Centrifuge and numerical modelling of normal fault-rupture propagation in clay with and without a pre-existing fracture. *J Geotech Geoenviron Eng* 2012;138(12):1492–502. [https://doi.org/10.1061/\(asce\)gt.1943-5606.0000719](https://doi.org/10.1061/(asce)gt.1943-5606.0000719).
- [16] Shen Chao, Bo Jingshan, Zhang Jianyi, et al. Application of geotechnical centrifuge technology in the study of fault movement. *J Nat Disasters* 2018;27(3):47–55. <https://doi.org/10.13577/j.jnd.2018.0306>.
- [17] White DJ, Take WA, Bolton MD. Soil deformation measurement using particle image velocimetry (PIV) and photogrammetry. *Geotechnique* 2003;53(7):619–31. <https://doi.org/10.1680/geot.53.7.619.37383>.
- [18] Chen Zhengfa, Yu Yuzhen. A review on development of geotechnical dynamic centrifugal model test. *Chin J Rock Mech Eng* 2006;25(z2):4026–33. <https://doi.org/10.3321/j.issn:1000-6915.2006.z2.108>.
- [19] Bransby MF, Davies MCR, El Nahas A, et al. Centrifuge modelling of reverse fault–foundation interaction. *Bull Earthq Eng* 2008;6(4):607–28. <https://doi.org/10.1007/s10518-008-9080-7>.
- [20] Zhou Qing, Xu Xiwei, Yu Guihua, et al. Investigation on widths of surface rupture zones of the M<sub>8.0</sub>Wenchuan earthquake, Sichuan Province, China. *Seismol Geol* 2008;30(3):778–87. <https://doi.org/10.3969/j.issn.0253-4967.2008.03.016>.
- [21] Xu Xiwei, Yu Guihua, Wentao M, et al. Evidence and methods for determining the safety distance from the potential earthquake surface rupture on active fault. *Seismol Geol* 2002;24(4):470–83. <https://doi.org/10.3969/j.issn.0253-4967.2002.04.001>.

- [22] Chen Yulong, Huang Dong. Centrifuge test of deformation characteristics of overburden clay subjected to normal and reverse fault rupture. *Rock Soil Mech* 2017;38(s1):195–200. <https://doi.org/10.16285/j.rsm.2017.S1.022>.
- [23] Stone KJL, Muir Wood D. Effects of dilatancy and particle size observed in model tests on sand. *Soils Found* 1992;32(4):43–57. [https://doi.org/10.3208/sandf1972.32.4\\_43](https://doi.org/10.3208/sandf1972.32.4_43).
- [24] Chang YY, Lee CJ, Huang WC, et al. Use of centrifuge experiments and discrete element analysis to model the reverse fault slip. *Int J Civ Eng* 2013;11(2):79–89. <https://doi.org/10.12989/sem.2013.48.3.415>.
- [25] Luo Guanyong, Ng CWW, Cai Qipeng. Centrifuge modelling of ground deformation induced by normal fault in saturated clay. *Rock Soil Mech* 2012;33(10):2985–3000. <https://doi.org/10.16285/j.rsm.2012.10.009>.